Editors' Suggestion

Topological nature of dislocation networks in two-dimensional moiré materials

Rebecca Engelke,[1] Hyobin Yoo,[2,3] Stephen Carr,[4] Kevin Xu,[1] Paul Cazeaux,[5] Richard Allen,[1] Andres Mier Valdivia,[6] Mitchell Luskin,[7] Efthimios Kaxiras,[1,6] Minhyong Kim,[8] Jung Hoon Han,[9] and Philip Kim[1,6]

[1]*Department of Physics, Harvard University, Cambridge, Massachusetts 02138, USA*
[2]*Department of Physics, Sogang University, Seoul 04107, Republic of Korea*
[3]*Institute of Emergent Materials, Sogang University, Seoul 04107, Republic of Korea*
[4]*Department of Physics, Brown University, Providence, Rhode Island, 02912, USA*
[5]*Department of Mathematics, Virginia Tech, Blacksburg, Virginia 24061, USA*
[6]*John A. Paulson School of Engineering and Applied Sciences, Harvard University, Cambridge, Massachusetts 02138, USA*
[7]*School of Mathematics, University of Minnesota, Minneapolis, Minnesota 55455, USA*
[8]*International Centre for Mathematical Sciences, Edinburgh EH8 9BT, United Kingdom*
[9]*Department of Physics, Sungkyunkwan University, Suwon 16419, Korea*

(Received 12 July 2022; revised 21 February 2023; accepted 23 February 2023; published 16 March 2023)

Moiré superlattice patterns at the interface of two-dimensional (2D) van der Waals (vdW) materials, arising from a small displacement between similar lattices, have been extensively studied over the past decade for their dramatic ability to tune material properties. However, previous work to understand the structure of these interfaces has largely focused on some special cases, particularly honeycomb lattices displaced by twist or isotropic scaling. In this work, we develop practical and analytical tools for understanding the moiré structure that can be generalized to other lattice distortions and lattice types. At large enough moiré lengths, all moiré systems relax into commensurated 2D domains separated by networks of dislocation lines. The nodes of the 2D dislocation line network can be considered as vortexlike topological defects. However, we find these topological defects to exist on a punctured torus, requiring different mathematical formalism than the topological defects in a superconductor or planar ferromagnet. In the case of twisted bilayer graphene, the defects are characterized by the free group on two generators. We find that antivortices occur in the presence of anisotropic heterostrain, such as a shear or anisotropic displacement, while arrays of vortices appear under a twist or isotropic displacement between vdW materials. Utilizing the dark field imaging capability of transmission electron microscopy (TEM), we experimentally demonstrate the existence of vortex and antivortex pair formation in a moiré system, caused by competition between different types of heterostrains in the vdW interfaces. We also present a methodology for mapping the underlying heterostrain of a moiré structure from experimental TEM data, which provides a quantitative relation between the various components of heterostrain and vortex-antivortex density in moiré systems.

DOI: 10.1103/PhysRevB.107.125413

I. INTRODUCTION

Moiré patterns are quasiperiodic in-plane projections of two similar stacked two-dimensional (2D) periodic lattices. Atomic scale moiré superlattices can be formed by stacking atomically thin van der Waals (vdW) materials; one such example is twisted bilayer graphene. Moiré patterns formed by incommensurately stacking 2D materials have been used to manipulate a system's electronic structure, from Hofstadter's butterfly [1–3] to the valley Hall effect [4,5] to magic angle strongly correlated physics [6,7]. As the number and type of layers in experimentally relevant systems proliferates, including twisted double bilayer [8–10], twisted monobilayer [11–13], twisted trilayer [14–16], and twisted quadrilayer graphene [17,18], as well as hexagonal boron nitride [19] and transition metal dichacolgenides (TMDs) [20–22], it is important to be able to predict the structure in vdW stacked combinations of atomic layers.

Increasing attention has been paid to the effects of strain disorder on the structure and properties of such systems [23]. The effect and extent of twist angle disorder in magic angle graphene is an active area of research [24,25]. Strained moiré patterns in excitonic systems have been proposed as a way to create 1D quantum wires [26]. In this paper, we present a generalizable topological interpretation of the structure of moiré interfaces that allows for the characterization of arbitrary strain and the proposition of new types of moiré patterns.

A topological description of the moiré structure is appealing in part because some of the major features of the structure seem to be fixed once certain boundary conditions, such as total twist angle and strain, are pinned. For large enough moiré length, moiré systems are known to relax into domains of nearly commensurate alignment, separated by domain walls which can be characterized as dislocation lines [27]. The topological connectivity of the network of dislocation lines remains fixed even as the domain lengths become distorted by local strain fields.

The nodes of the network where dislocation lines meet in the relaxed moiré system (sometimes known as AA points in graphene or TMD moiré) have been referred to as topological

defects by Alden *et al.* [28], and again by Turkel *et al.* [29], who also emphasize their role in transport as tunable, local concentrations of twist angle. They have also been shown to play the role of defects in electrochemistry [30]. However, we find that the order parameter describing the topology of these defects is rather different from that of the conventional vortex descriptions in the planar magnet or superfluid, where the order parameter can be described by a complex number.

The complex order parameter space can be mapped to a circle (S^1), hence the fundamental group is $\pi_1(S^1) = \mathbb{Z}$. The fundamental group is a useful tool in the analysis of topological defects, as defects and their collections can each be mapped to an element of the fundamental group [31]. For defects with an S^1 order parameter, this manifests as an integer winding number [32]. Interestingly, we find that the order parameter space describing the relaxation structure of a moiré superlattice is not homotopy equivalent to S^1 due to the periodic boundary condition of the order parameter imposed by the moiré superlattice. We present a mathematical framework, similarly based on the fundamental group, by which the 2D dislocation network nodes can be characterized as topological defects.

Throughout the paper, we refer to the space of order parameters as *configuration space*, in keeping with the convention adopted in earlier works [33]. For most of this work, we focus on graphenelike moiré superlattices, where two different domain types, AB and BA, are separated by dislocation lines meeting at the AA site. The starting point for our new vortex description of the AA nodes is the realization that the configuration space for the graphenelike moiré superlattice is the *punctured torus*. The fundamental group of the punctured torus is a non-Abelian group known as F_2, the free group on two generators. The commutator $[a, b] = aba^{-1}b^{-1}$ corresponds to a closed loop around a vortex centered at the AA node of the moiré superlattice (its inverse $[b, a] = [a, b]^{-1}$ corresponds to a path around an antivortex). The noncommutativity of the generators is a consequence of the removed point at the AA node, which is physically motivated by the node's high energy barrier in the generalized stacking fault energy [33].

The domain walls that emerge in the moiré superlattice will be color-coded as R, G, B, which correspond to the three distinct ways in which the AB stacking order makes a transition to the BA stacking order as the domain wall is crossed. The aforementioned generators a and b can be related to the *RGB* color coding of the domain walls, which are experimentally accessible quantities. Examination of the color distribution of domain walls crossing an arbitrary closed boundary reveals the vortex content enclosed within, according to the non-Abelian vortex theory developed here. The use of the free group language to characterize the topological structure of a moiré superlattice is likely to find application in other kinds of superlattices formed from incommensurate stacking of nonhexagonal crystals, with details of the group determined by the material-dependent stacking energy profiles and lattice symmetry.

As mentioned before, the non-Abelian vortices in a moiré superlattice have a counterpart in non-Abelian antivortices. We find that the relative strain tensor between two constituent layers determines the vortex/antivortex distribution of the sample. The mathematical tools to understand configuration space combined with experimental information on the configuration distribution in real space enables us to estimate the strain distribution underlying a moiré pattern, allowing for the characterization or engineering of strain distributions in van der Waals heterostructures.

The remainder of the paper is organized as follows. In Sec. II, we go over various tools and concepts used in analyzing the strain patterns and the nature of topological defects in the moiré superlattice. The notion of theta space as the proper configuration space of the graphenelike moiré superlattice is introduced and justified by energetic consideration. Section III discusses the formal theory of the vortex and antivortex in a moiré superlattice using the language of the free group and its generators. The mathematical discussion is followed by Sec. IV in which the new algebraic formulation of vortices and anti-vortices is employed to identify antivortex formation in a real moiré superlattice, by way of a novel method of strain mapping. Section V gives a summary and discussion. Technical details of the theory of vortex algebra are included in Appendixes A and B with the hope that future investigations of moiré superlattices, including lattices other than sublattice-symmetric honeycomb lattices, can make use of the type of vorticity formulation presented here. Appendix C includes details on the image processing to experimentally measure the lattice displacement.

II. ORDER PARAMETER AND CONFIGURATION SPACE FOR MOIRÉ SUPERLATTICE

The natural choice of order parameter in a bilayer system is the local shift vector, $\mathbf{u}$, determined as the in-plane vector that points from a lattice site in one layer to the equivalent lattice site in the other layer. Figure 1 illustrates of how we define the shift vector in a graphenelike honeycomb lattice. Because of the periodicity of the lattice, a shift vector larger than a unit cell, as shown in Fig. 1(b), is equivalent to the shorter vector folded into the first unit cell. In other words, the configuration space in which this order parameter exists is a torus [33].

After labeling the two honeycomb lattice sites as A and B, the standard naming convention for the bilayer honeycomb stackings is obtained by listing the pair of vertically aligned sites. The condition $\mathbf{u} = 0$, when every atom is on top of an equivalent atom in the other layer, is known as AA stacking. Shifting the top layer along one of the three atomic bonds from an A site to a B site of the other layer [Fig. 1(d)], or along the negative of those three vectors [Fig. 1(c)] yields a structure where only half the atoms in the top and bottom layers coincide in the 2D projection. The latter two stacking configurations are often termed AB and BA stacking, respectively. In graphene, the AA stacking is energetically unfavorable, while the AB and BA stackings are symmetry-related lowest-energy layer stacking configurations, called Bernal stacking. Note that for each of the two graphene Bernal stacking configurations, three different shifting directions result in the same stacking configuration, represented by a single point on the toroidal configuration space. AB and BA stacking are connected by spatial inversion, leading to $\mathbf{u}_{\mathrm{AB}} = -\mathbf{u}_{\mathrm{BA}}$ for the corresponding shift vectors in the configuration space [Fig. 1(e)]. The high-energy nature of the AA stacking can

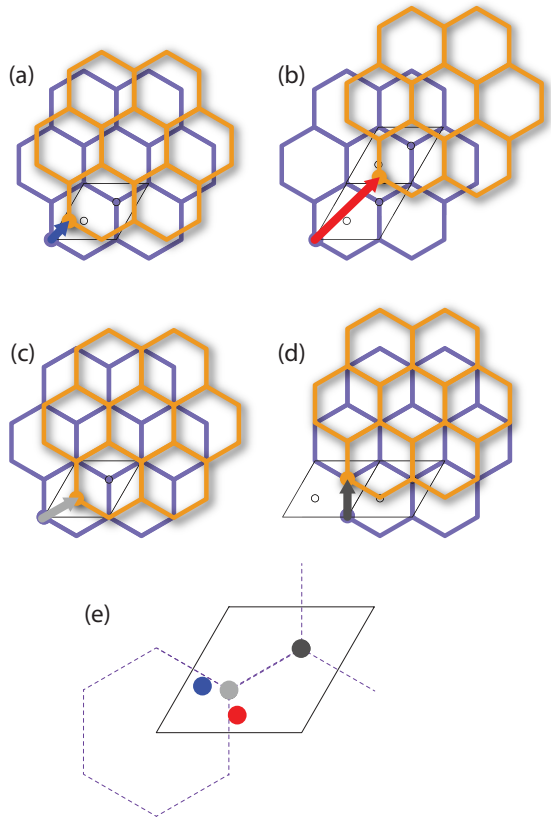

FIG. 1. (a)–(d) Definition of shift vector: (a) small shift, (b) shift larger than a unit cell is mapped into the first unit cell, (c), BA shift (d) AB shift. (e) Shifts from part (a) shown in configuration space. Dotted lines show an alternate Wigner–Seitz-like designation of the configuration space unit cell.

be reflected by removing $\mathbf{u} = 0$ from the configuration space altogether, rendering the topology from that of a torus to that of a punctured torus. This will play a crucial role in the theory of vorticity we develop in Sec. III.

Figure 1(e) shows the points in configuration space corresponding to the real-space configurations in (a)–(d). The high symmetry stackings, BA and AB, are represented by the dark gray and light gray points in Fig. 1(e), respectively. As the unit cell can be defined in various ways, it is equally valid to use the parallelogram definition of the unit cell shown in Fig. 1, where AA is the corner, or the hexagonal unit cell shown in dotted lines, in which AB and BA are corners of the hexagon.

A. Experimental measurement of order parameter

Transmission electron microscopy (TEM) provides an experimental route to characterizing local atomic configurations in real space, including detecting the change in $\mathbf{u}$ across a domain wall, known as the Burgers vector. Changes in the stacking order are distinguishable by a dark field imaging technique that consists of inserting an aperture into the diffraction plane around a single Bragg position and recording the resulting filtered real space image. Depending on the choice of diffraction peak, contrast between domains [see Fig. 2(a)] or the partial dislocations that form the domain walls [see Fig. 2(b)] in the bilayer stacking are visible [28]. The Burgers

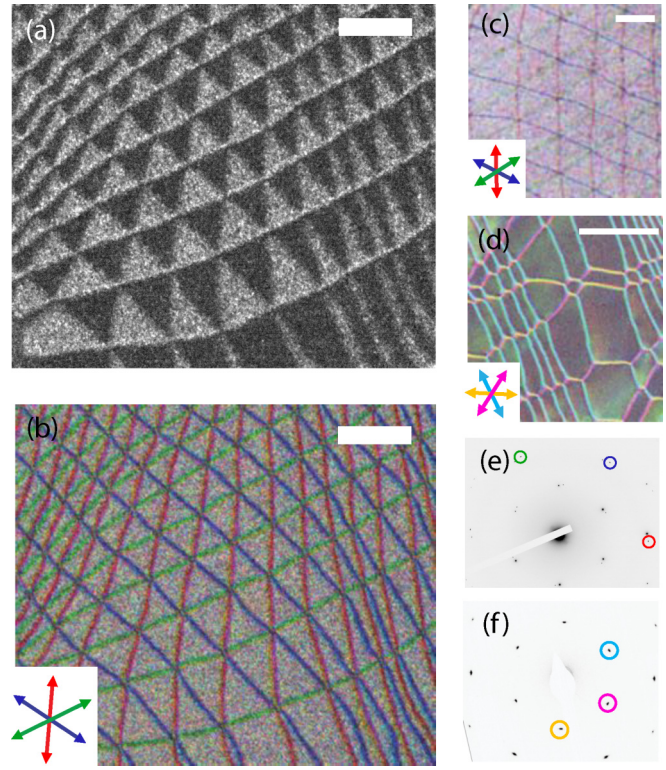

FIG. 2. Dark field TEM images. (a) $\{10\bar{1}0\}$ ("first order") dark field of twisted bilayer graphene, showing domain contrast. (b) $\{11\bar{2}0\}$ ("second order") dark field of the area in (a) showing domain walls meeting at sixfold nodes. (Inset) Burgers vectors corresponding to domain wall colors. (c) Second order dark field of MoS_2 twisted from 3R-like stacking has a similar network topology to graphene. (Inset) Burgers vectors corresponding to domain wall colors. (d) $\{10\bar{1}0\}$ dark field of MoS_2 twisted from 2H-like stacking has a threefold network topology. (Inset) Burgers vectors corresponding to domain wall colors. (e) Diffraction pattern of the sample in (a) with colors of second order diffraction spots circled. Sample (c) has a similarly oriented diffraction pattern. (f) Diffraction pattern of the sample in (d) with the colors of first order diffraction spots circled. Scale bars are 100 nm.

vectors of the dislocations are exactly determinable, as the vector perpendicular to the diffraction peak for which their contrast vanishes in the dark field image [28,34]. The Burgers vector of a dislocation in the bilayer is equal to $\Delta\mathbf{u}$, the change in shift vector across the boundary.

We note that the dislocations form a network with distinct topology. Twisted bilayer graphene [Fig. 2(b)] has a structure where six dislocation lines meet at a node. Despite being a different material with different symmetries, MoS_2 slightly twisted from a 3R-like stacking (close to 0° twisting) appears to share the same dislocation network topology as graphene [Fig. 2(c)]. In contrast, MoS_2 twisted from a 2H configuration (close to 180° twisting) has a structure where three lines meet at a node rather than six [Fig. 2(d)]. As we will explore later, the topology of the graphene and 3R-like case is defined by a punctured torus, originating from the single energy maximum in the stacking fault energy as a function of configuration (and two degenerate minima). However, for twisted 2H MoS_2 there are two energy maxima and one minimum, leading the

configuration space to be described as a twice-punctured torus and generating a different topology. While in this paper we focus on the topology generated by the energy profile of bilayer graphene, we are motivated by the realization that a topological description of each system's configuration space should distinguish the different possible connectivities of the network, including those arising from materials of different lattice symmetry, such as a square lattice.

While constructing the tools to analyze the topological defects of the moiré superlattice in configuration space, we also attain the ability to analyze the configuration distribution and extract the overall strain profile in the twisted bilayer. In order to do these analyses, we need to consider several important quantities of the moiré lattice: the displacement gradient matrix, the moiré vectors, and the Burgers vectors. All of these quantities give important information that allows us to reconstruct $\mathbf{u}$.

B. Displacement gradient matrix

A displacement vector field $\mathbf{u}$ which describes the shift in positions of a lattice ($\mathbf{x}_t$) compared to a reference lattice ($\mathbf{x}_b$) such that $\mathbf{x}_t = \mathbf{x}_b + \mathbf{u}(\mathbf{x}_b)$, is closely related to strain. Typically, $\mathbf{x}_t$ is a 2D vector corresponding to the positions in the strained lattice, and $\mathbf{x}_b$ is a 2D vector corresponding to the positions in the intrinsic lattice, prior to application of forces. In the case of moiré materials, presented in Fig. 1, the reference lattice (with coordinates $\mathbf{x}_b$) is the bottom layer of the material, and the displaced lattice ($\mathbf{x}_t$) is the top layer. Thus the vector field that produces a moiré pattern is in a sense analogous to the relative strain (heterostrain) between the two layers.

The linear strain matrix, used in the modeling of strain energies, is defined by taking derivatives of the $\mathbf{u}$ field and symmetrizing:

$$\varepsilon = \begin{pmatrix} \partial_x u_x & (\partial_y u_x + \partial_x u_y)/2 \\ (\partial_y u_x + \partial_x u_y)/2 & \partial_y u_y \end{pmatrix}. \tag{1}$$

Note that this symmetrized linear strain tensor does not contain rotation contributions to first order in angle, since rotation of a lattice is just a coordinate change and does not contribute strain.

If we do not symmetrize, i.e., keep the rotation component, the gradient of the $\mathbf{u}$ field is known as the displacement gradient matrix, $\overline{d}$, obtained from

$$\overline{d} = \nabla \mathbf{u} = \begin{pmatrix} \partial_x u_x & \partial_y u_x \\ \partial_x u_y & \partial_y u_y \end{pmatrix}. \tag{2}$$

The vector $\mathbf{u}$ can be recovered by integrating $\overline{d}$ over distance. If we assume that $\mathbf{u}(0) = 0$ and that the strain is spatially uniform from $\mathbf{0}$ to $\mathbf{x}_b$, we obtain

$$\mathbf{u}(\mathbf{x}_b) = \overline{d}\mathbf{x}_b. \tag{3}$$

Thus $\mathbf{x}_t = \mathbf{x}_b + \overline{d}\mathbf{x}_b$ or

$$\mathbf{x}_t = (1 + \overline{d})\mathbf{x}_b \tag{4}$$

Any arbitrary displacement of layer 2 relative to layer 1, formed by a combination of twist and strain, can be written in terms of a displacement gradient matrix, $\overline{d}$, with four independent components. It is useful to define the four components as follows:

$$\overline{d} = \begin{pmatrix} \alpha + \beta & \gamma - \theta \\ \gamma + \theta & \alpha - \beta \end{pmatrix}, \tag{5}$$

where θ is a linear approximate of the twist (measured in radians), α is isotropic strain, and β and γ are uniaxial and shear strain, respectively [35].

C. Moiré length

The moiré length is the distance over which the lattice $\mathbf{x}_t$ has been shifted by a unit vector with respect to lattice $\mathbf{x}_b$, creating a local return to the starting configuration.

Consider the shift vector $\mathbf{u}$, as defined in Fig. 1. If we twist our lattices about a point where two atoms are stacked on top of each other, the origin has $\mathbf{u} = 0$. Traveling away from the origin in a direction $\mathbf{x}$, the displacement $\mathbf{u}$ increases until we reach the point where the lattices have diverged by a whole unit cell ($\mathbf{u} = \pm\mathbf{a}_1$ or $\pm\mathbf{a}_2$, where $\mathbf{a}_1$ and $\mathbf{a}_2$ are two lattice vectors of the unstrained lattice) and thus are aligned ($\mathbf{u} = 0$) again, resulting in moiré periodicity.

A general interface of 2D lattices with heterostrain, $\mathbf{x}_t = (1 + \overline{d})\mathbf{x}_b$, can be characterized by a pair of moiré vectors, $\mathbf{m}_i$ ($i = 1, 2$), which describes the moiré periodicity in the 2D space. Considering the corresponding pair of two coincident lattice points in the upper and lower layers, $\mathbf{x}_{t,i}$ and $\mathbf{x}_{b,i}$, respectively, the two moiré vectors can be expressed

$$\mathbf{m}_i = \mathbf{x}_{t,i} = \mathbf{x}_{b,i} + \mathbf{s}_i, \tag{6}$$

where the constant vectors $\mathbf{s}_i$ can each be $\pm\mathbf{a}_1$ or $\pm\mathbf{a}_2$, depending on the coincident lattice condition for the moiré superlattice.

If $\mathbf{s}_1$ and $\mathbf{s}_2$ are collinear (without $\mathbf{m}_1$ and $\mathbf{m}_2$ being collinear), then the matrix $\overline{d}$ has determinant zero and the moiré pattern is 1D rather than 2D. We will ignore this case for now, and assume that $\mathbf{a}_1$ and $\mathbf{a}_2$ are each used once.

We can relate the lattice constants $\mathbf{a_i}$, the matrix $\overline{d}$ and the moiré vectors, by $\mathbf{m}_i = \mathbf{x}_{t,i} = (1 + \overline{d})\mathbf{x}_{b,i}$. Thus if $\overline{d}$ is invertible, $\mathbf{x}_{b,i} = \overline{d}^{-1}\mathbf{s}_i$ and

$$\mathbf{m}_i = (1 + \overline{d}^{-1})\mathbf{s}_i. \tag{7}$$

Putting Eq. (7) together with the corresponding equation for the other moiré vector, $\mathbf{m}_i$, we obtain a matrix equation that can be solved for $\overline{d}$ if we have measured $\overline{m}$ and $\overline{s}$:

$$\overline{m} = (1 + \overline{d}^{-1})\overline{s}, \tag{8}$$

where $\overline{m}$ and $\overline{s}$ are 2×2 matrices formed by horizontally concatenating the $\mathbf{m}_i$ and $\mathbf{s}_i$ column vectors, respectively. Note that if the two $\mathbf{m}_i$'s are not linearly independent, that is again the $|\overline{d}| = 0$ case.

D. Burgers vector

The shift vector $\mathbf{u}$ is also related to the Burgers vector of the dislocations that form in the relaxed moiré system. To define the Burgers vector, first one considers a closed path

along the lattice points of a perfect crystal, sometimes called a Burgers circuit. When a dislocation is introduced within this path the circuit becomes broken, and the vector connecting the now separated start and end points of the circuit is called the Burgers vector. In a moiré superlattice, the twisted interface acts as a dislocation, and we can obtain Burgers vectors by considering circuits that traverse the interface. The simplest closed circuits in the aligned, untwisted structure take the following form: travel from a lattice point $\mathbf{x}_0$ to $\mathbf{x}_1$ along the top layer, then down vertically into the bottom layer, then along $\mathbf{x}_1$ to $\mathbf{x}_0$ in the bottom layer, and finally return to $\mathbf{x}_0$ in the top layer by moving vertically upwards. To connect the Burgers vector $\mathbf{b}$ to the shift vector $\mathbf{u}$, it is easiest to think of obtaining the twisted geometry by keeping the bottom layer fixed and introducing a dislocation via rotation of the top layer. In this case, the failure of the circuit to close after applying the twist is equal to the relative change in positions of the lattice points that corresponded to $\mathbf{x}_0$ and $\mathbf{x}_1$ in the top layer. However, this is simply the change in the local shift between the two points, e.g.,

$$\mathbf{b} = \int_{\mathbf{x}_0}^{\mathbf{x}_1} (d\mathbf{x} \cdot \nabla)\mathbf{u}(\mathbf{x}) = \mathbf{u}(\mathbf{x}_1) - \mathbf{u}(\mathbf{x}_0), \tag{9}$$

where the nonintegral form is only true if one does not map $\mathbf{u}$ into the compact unit-cell torus.

While this expression was obtained under the assumption of a uniformly twisted system, the result is quite general. For the relaxed systems that occur in experimental devices, one finds that the Burgers vector is only nonzero if a "dislocation line" (that is, a domain wall) is enclosed in the circuit. Each dislocation line between a pair of AA nodes can be associated with a specific Burgers vector, as was done experimentally using DF TEM in Fig. 2. The pair of AA nodes also provides a moiré vector $\mathbf{m}_i$, which can be linked to $\mathbf{s}_i$ obtained from the Burgers vectors. Therefore knowledge of the moiré vectors $\mathbf{m}_i$ and the Burgers vectors across the dislocations associated with $\mathbf{m}_i$ is sufficient to solve for the displacement gradient matrix using Eq. (8). As the moiré vectors and Burgers vectors can be measured from experimental dark field and diffraction images, it is possible to obtain a map of $\overline{d}$ from the information provided by DF TEM images, as we will discuss in Sec. IV B.

E. Configuration space

Although a torus is topologically nontrivial, a small loop around the AA site ($\mathbf{u} = 0$) on the torus can be contracted to a point and thus does not inherit any nontrivial topological properties from the torus. The topological defects associated with winding around the holes of the torus are the dislocations [32], but this description alone provides no constraint on the manner in which the dislocations meet at the nodes. In the case of a graphene moiré superlattice, the three dislocation lines with different Burgers vector, colored red (R), green (G), and blue (B), converge at the AA defect and diverge out again. What we need is a proper mathematical description of the topological nature of the AA nodes consistent with the experimental findings.

We start by investigating the distribution in configuration space of the order parameter for unrelaxed and relaxed moiré systems. Figure 3(a) shows an unrelaxed twisted bilayer of

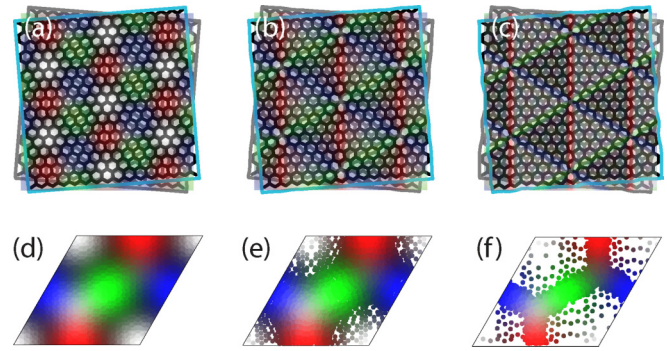

FIG. 3. [(a)–(c)] Schematic of real space arrangement for (a) unrelaxed moiré structure, (b) partially relaxed moiré structure, and (c) fully relaxed moiré structure. Colors denote region in configuration space corresponding to local stacking order. [(d)–(f)] Distribution in configuration space of local stacking order sampled at each plaquette of the lattice for (d) unrelaxed moiré structure, (e) partially relaxed moiré structure, and (f) fully relaxed moiré structure.

a honeycomb lattice, and Fig. 3(d) shows the configuration space, colored via a scheme that is used consistently throughout this work. A Gaussian intensity distribution of a chosen color is centered around each key point in configuration space. The region of configuration space centered around the AA point is colored white, and those centered around AB (BA) are dark gray (light gray). Red, green, and blue regions are placed on the midpoint of the three equidistant shortest paths between AB and BA, two of which require crossing the unit cell boundaries. The coloring in real space in Figs. 3(a)–3(c) is determined for each point, by determining the local shift vector, finding it as a point in configuration space, and adopting the color corresponding to that point.

Figures 3(b) and 3(c) depict real space structures that have been modulated by a periodic lattice distortion to mimic relaxation, with two different amplitudes. As the amplitude of relaxation is increased from Fig. 3(a) to 3(b) to 3(c), light or dark gray regions, corresponding to nearly AB or BA stacking, take up increasing areas in real space, while AA regions shrink, and red, green, and blue regions evolve into lines. Because the red, green, and blue color tell us which path on the torus was used to get between BA and AB, i.e., $\Delta\mathbf{u}$, the color tells us the Burgers vector of that line. The corresponding distributions in configuration space are shown in Figs. 3(d)–3(f). As relaxation strength increases, decreasing point density around the AA configuration reveals that fewer points in real space correspond to AA stacking, while configurations on the red, green, and blue lines, and especially AB and BA sites, become more numerous. Thus, the atomic lattice relaxation process in real space can be viewed as emptying out most of configuration space and populating only the AB and BA points and dislocation lines connecting them.

A similar emptying of AA and concentration at AB, BA, and the colored lines between AB and BA, occurs for the three strain types: isotropic, uniaxial, and shear. Figures 4(a)–4(c) show the configurations formed by $\mathbf{x}_t = (1 + \overline{d})\mathbf{x}_b$ with a spatially constant displacement gradient matrix $\overline{d}$, corresponding to only one nonzero component α, β, or γ in Eq. (5).

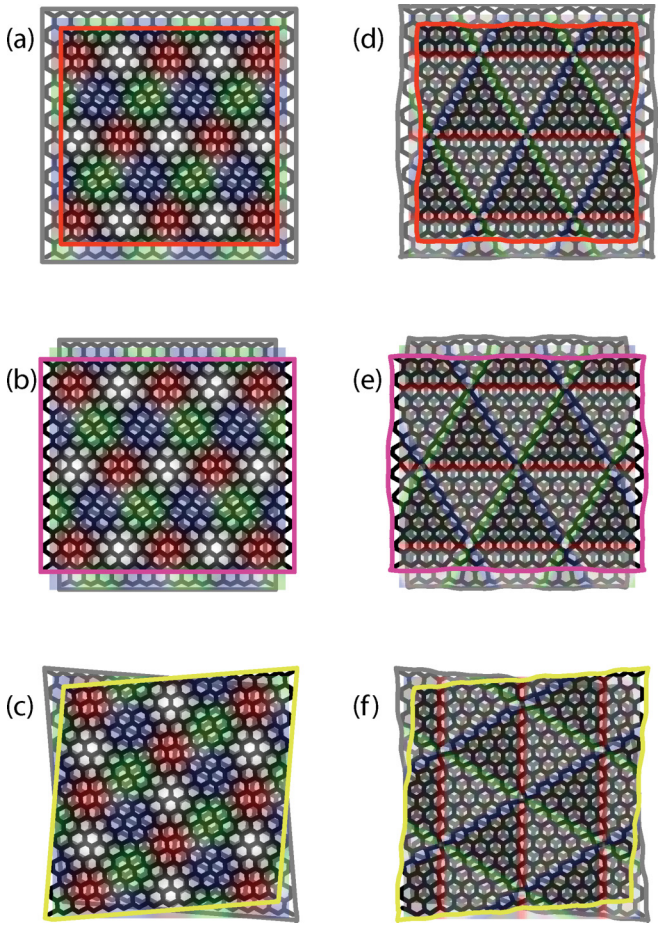

FIG. 4. Schematics of real space structure for the three strain components. Moiré from (a) isotropic scaling, (b) uniaxial strain, and (c) shear strain. Relaxed moiré from (d) isotropic scaling, (e) uniaxial strain, and (f) shear strain. Colors correspond to configurations, as defined in Fig. 3.

Figs. 4(d)–4(f) show corresponding structures after applying the modulation function to mimic atomic scale relaxation. We note that the order and orientation of red, green, and blue lines differs in real space for each strain component, as well as twist. In this sense, the colors (encoding local order parameter) provide information about which strain components are present.

III. THEORY OF DISLOCATION NETWORK NODES IN MOIRÉ SUPERLATTICES

As emphasized previously, the proper order parameter space for a moiré superlattice and the various network structures observed in it is the space of shift vectors $\mathbf{u}$ with the boundary conditions of a torus and one point $\mathbf{u} = 0$ removed due to energy considerations (and the ensuing atomic relaxation), as shown in Fig. 5(b). But the TEM images shown in Fig. 2 suggest an even more constrained space for the order parameter. For moiré regions with a sufficiently large moiré length scale, the order parameter is locked to either the AB ($\mathbf{u}_{AB}$) or BA ($\mathbf{u}_{BA}$) point in the configuration space. There are three equivalent ways to make a transition from BA to AB stacking orders, designated by red, blue, and green arrows

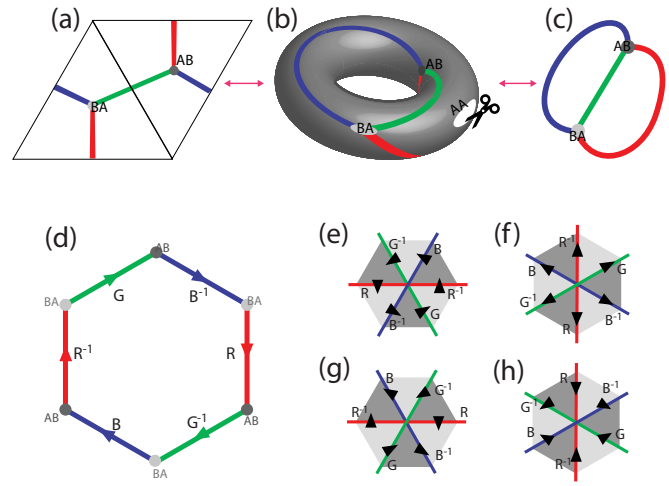

FIG. 5. Energy landscape in the configuration space torus determines the topology of the network, which can be equivalently viewed (a) on the unit cell, (b) as a torus with a puncture (AA configuration is removed from space), or (c) as theta space. (d) Using the hexagonal unit cell, it can be seen that clockwise or counterclockwise paths around an AA point determine the order in which *R*, *G*, and *B* elements are encountered. [(e)–(h)] Real space arrangement of dislocations corresponding to clockwise paths in configuration space, generating vortices [(e) and (f)] and counterclockwise paths in configuration space, generating antivortices [(g) and (h)]. Each domain wall is colored and labeled based on the R, G, or B move in configuration space. The direction of the configuration space move, equivalent to the Burgers vector, is shown by the black arrows. Comparison with Fig. 4 identifies the structures as generated from: (e) isotropic, (f) twist, (g) uniaxial, and (h) shear displacement.

in Fig. 5(d) with corresponding label *R*, *G*, and *B*. The AB to BA transition is accomplished by their inverses, shown as R^{-1}, G^{-1}, and B^{-1} in Fig. 5(d). Since the $\mathbf{u}_{AB}$, $\mathbf{u}_{BA}$, and the three *RGB* lines connecting the two points span the entirety of the relevant order parameters, one can "gouge out" the unnecessary portions of the punctured torus. The result is the theta space shown in Fig. 5(c). This is the relevant configuration on which to make a proper definition of vorticity, not the circle (S^1) where the usual homotopic classification of vorticity takes place [32].

Before developing the formal theory of vorticity in the next section, we complete the phenomenological classification of possible vortex patterns around the AA node. According to the TEM data, a path around a single AA node in real space simultaneously implies encircling the AA spot in configuration space by $\mathbf{u}$. Closed paths in real space that encircle a node of the dislocation network now correspond to noncontractible paths in configuration space. The vortex winding number w can be intuitively defined as $+1$ or -1 if the configuration space loop cycles the same or opposite direction as the real space loop, respectively [Fig. 5(d)]. Recalling that the red, green, and blue paths in configuration space correspond to Burgers vectors of dislocations in real space, the possible orderings of Burgers vectors in real space surrounding an AA node can be determined. There are four distinct arrangements: starting at either AB or BA in Fig. 5(d), one can circle either clockwise [$w = +1$, Figs. 5(e) and 5(f), describing vortices]

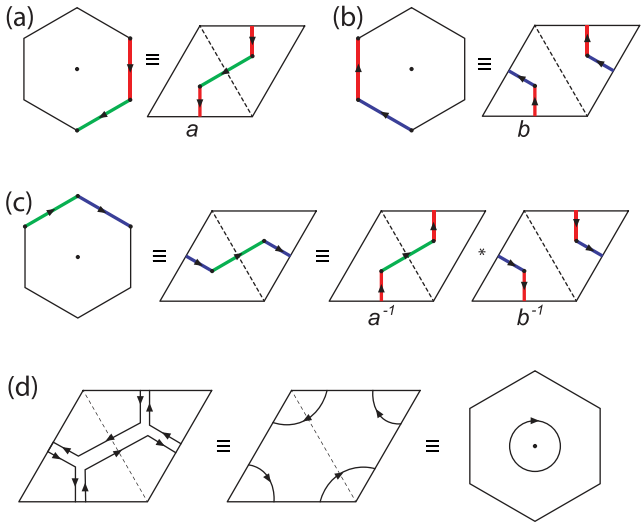

FIG. 6. (a) The RG^{-1} move in the hexagonal zone scheme of the configuration space is translated into a noncontractible loop in the parallelogram zone scheme. It is labeled by a. (b) The BR^{-1} move in the hexagonal zone scheme of the configuration space is translated into a second noncontractible loop in the parallelogram scheme. It is labeled by b. (c) The GB^{-1} move in the hexagonal zone scheme is translated into a third noncontractible loop that can be decomposed as a product of the previous two moves, $a^{-1}b^{-1}$. (d) The $aba^{-1}b^{-1}$-loop is equivalent to a circle round the point $\mathbf{u} = 0$. It is a noncontractible loop due to the high-energy barrier for the $\mathbf{u} = 0$ configuration.

or counterclockwise [$w = -1$, Figs. 5(g) and 5(h), describing antivortices]. Comparing the locations of red, green, and blue lines in Figs. 5(e)–5(h) and in Fig. 4, it can be concluded that twist and isotropic strain produce vortex-type defects at the nodes, and uniaxial or shear strain produce antivortex-type defects at the nodes. Note that reversing the direction of twist or exchanging layers does not convert vortices into antivortices. The only way to produce antivortices is to have an anisotropic heterostrain between the layers.

A. Algebraic formulation of vorticity

To understand the algebraic structure of paths in the theta space [Fig. 5(c)], it is useful to consider the same path through configuration space in both the unit-cells shown in Fig. 1(e). Let us consider the full encirclement of the AA node shown in Fig. 5(d). We begin by observing that the BA $\rightarrow$ AB $\rightarrow$ BA transition through the R and G^{-1} dislocations in Fig. 5(d) becomes, in the parallelogram scheme shown in Fig. 6(a), a noncontractible loop about the torus' periodic boundary conditions. The other BA $\rightarrow$ AB $\rightarrow$ BA transition through the B and R^{-1} arrows in the hexagonal scheme becomes another noncontractible loop in the parallelogram unit cell shown in Fig. 6(b). We label the first and the second transitions as a and b, which will soon be identified with two generators of the free group F_2 [36,37]. The third BA $\rightarrow$ AB $\rightarrow$ BA move through G and B^{-1} arrows of the hexagon can be decomposed as the inverse of a followed by the inverse of b, or $a^{-1}b^{-1}$ [Fig. 6(c)]. A complete loop around the edges of the hexagonal unit cell is equivalent to the algebraic operation $aba^{-1}b^{-1} \equiv [a, b]$. Our convention is to perform the operation appearing on the left side of the product first.

The commutator $[a, b]$ in the language of the free group with two generators a, b represents a "vortex" centered about the AA defect. The vorticity of this topological defect can naturally defined as the commutator $[a, b]$ (more detailed discussion in Appendix A). Similar to the conventional vortex defined in S^1, this vorticity defined for the AA node is nontrivial in the sense that it is not contractible to an identity, as illustrated in Fig. 6(d). After canceling out the paths that are traversed both ways, the overall path for $[a, b]$ becomes equivalent to four partial loops around the four corners of the parallelogram, equal to a full loop round $\mathbf{u} = 0$. On a torus such a loop can be contracted to zero and become trivial, but not for a punctured torus. The antivortex has the algebraic representation $[b, a] = bab^{-1}a^{-1} = [a, b]^{-1}$. Geometrically, this amounts to starting from the same BA point on the upper left corner of the hexagonal unit cell in Fig. 5(d) and making a complete counter-clockwise loop. Appendix A gives a more complete account of the vortex structures in the language of free groups with two generators a, b. One can find group-theoretic representations for vortex dipoles (vortex + antivortex) and vortex quadrupoles (two vortices and two antivortices) as well.

B. RGB formulation of vorticity

As we described in Sec. II A, dark field TEM imaging can identify the dislocation lines with given Burgers vectors and the AB and BA domains separated by them. Each dislocation line converging on a given AA node can then be color-coded as R, G, B or one of their inverses R^{-1}, G^{-1}, B^{-1} considering Burgers vector and the neighboring AB/BA domains in the TEM measurement. The free group language of the previous subsection gives a mathematically complete account of the vortex and antivortex structures, but it is helpful to translate the same statement to the more tangible and experimentally measurable RGB scheme according to

$$a \leftrightarrow RG^{-1},\ b \leftrightarrow BR^{-1}\ ba \leftrightarrow BG^{-1}. \tag{10}$$

By direct substitution, we obtain the commutator

$$[a, b] = RG^{-1}BR^{-1}GB^{-1}, \quad \text{(vortex)} \tag{11}$$

which is a product of transition vectors over the six domain walls in succession. In the same scheme, we have the antivortex commutator

$$[b, a] = BG^{-1}RB^{-1}GR^{-1} \quad \text{(antivortex)}. \tag{12}$$

Any cyclic permutation of the six letters gives rise to the equivalent vortex or antivortex.

While the sign of the exponent in R, G, and B operators can be obtained considering the order of the neighboring AB and BA domains by combining the DF TEM images with the first and second order Bragg peaks as shown in Fig. 2, there is a simpler scheme to assign the sign of the operators, considering AB/BA domains are always complementary. For example, if the six dislocation lines converging on an AA node appear, for instance, in the order of $RGBRGB$ while going clockwise around it, it ought to be interpreted as $RG^{-1}BR^{-1}GB^{-1}$ given

in Eq. (11) and classified as a vortex. If the colors appear as *RBGRBG*, it is an anti-vortex according to Eq. (12). One only needs to keep in mind that the sequence of colors is to be understood as one color letter followed by the inverse of another color letter, and vice versa. Generalizations of the RGB scheme to vortex-antivortex dipole and/or vortex quadrupole structure are discussed in the Appendix B.

IV. EXPERIMENTAL OBSERVATION OF ANTIVORTICES AND STRAIN

A. Detection of antivortices

While moiré patterns and commensurated domain systems with vortex-type nodes have been studied extensively, those with antivortex-type nodes have not been demonstrated. We postulate this is due to the energy required to maintain sufficient strain, whereas twist and lattice constant mismatch can create vortex-type moiré without global strain. Nonetheless, we observe a line of antivortex nodes along a boundary of nonuniformly strained moiré superlattice.

Figure 7(a) shows combined DF TEM images of a twisted bilayer graphene sample that contains a ∼1 μm sized bubble formed underneath the sample. Near the boundary of the bubble, nonuniform relative strain builds up in the moiré superlattice, which in turn creates the various strain components discussed in Eq. (5). The antivortices (vortices) can be identified by the *RBG* (*RGB*) order in which the dislocations occur in a clockwise loop. The antivortices, which form along the top edge of a closed-loop dislocation, are each capable of annihilating with a nearby vortex, keeping the net winding number w constant within a fixed-boundary region. In Fig. 7(b), loop A surrounds a vortex-antivortex pair, with $w = 0$. Loop D, which surrounds the entire closed-loop dislocation, also has net $w = 0$ as the entire feature could annihilate if the local strain were removed, in which case it would become similar to loop E. When circling a single antivortex (B) or vortex (C), the winding number is nonzero.

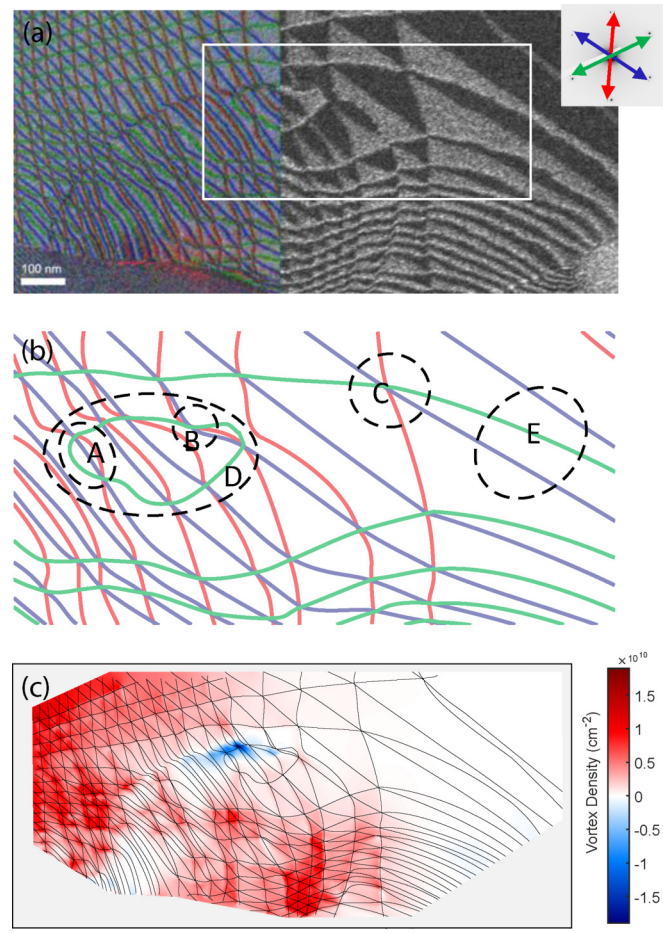

FIG. 7. (a) Dark field image of twisted bilayer graphene containing antivortices along a bubble edge. Left region shows colored second order image, right region shows first order image. (Inset) Burgers vector directions corresponding to dislocation colors, superimposed on diffraction pattern. (b) Zoom in on tracing of region of white box in 1a. Loops are drawn and topological number of each loop is counted. (A) Vortex-antivortex pair, $w = 0$. (B) Antivortex, $w = -1$. (C) Vortex, $w = +1$. (D) Closed-loop dislocation, $w = 0$. (E) Linear domains, $w = 0$. (c) Vortex density map computed from interpolated displacement gradient matrix of image (a)

B. Strain mapping

Existence of antivortices is a measure of the fact that anisotropic strains (uniaxial and shear) are dominating over the isotropic and twist components. Anisotropic strains alter the band structure and can produce pseudomagnetic fields [38]. We can quantify the various strain components from the displacement gradient matrix. Computation of the displacement gradient matrix from a DF TEM image is discussed in Appendix C. In brief, one component of the order parameter is known at every colored line, and an elastic model is used to interpolate in between, obtaining an estimate of the order parameter in the continuum. The displacement gradient matrix can be obtained by differentiating the order parameter. This method can be readily applied to any DF TEM images with prominent relaxation effect, such that the dislocation lines and their nodes are identifiable. For twisted graphene, this corresponds to angles approximately 1° and below [27].

The density of vortices or antivortices is computed in Fig. 7(c), by taking the determinant of the displacement gradient matrix, $|\bar{d}|$, which by the definition in Eq. (5) is equal to $(\alpha^2 + \theta^2) - (\beta^2 + \gamma^2)$ in terms of the strain and twist components. If $|\bar{d}| > 0$, vortices are present and if $|\bar{d}| < 0$, antivortices are present (see Appendix C). Thus, if the isotropic components (twist and isotropic scaling) outweigh the anisotropic components (shear and uniaxial strain), vortices form, and if the opposite, antivortices form. If $|\bar{d}| = 0$, 1D domains are observed [26,39].

We further use our estimated displacement gradient matrix to create strain maps of the three strain components, plus twist. Note that the moiré pattern only provides information on the heterostrain, or difference in strain between the two lattices. Furthermore, in this work, we are interested in the large-scale strain pattern that leads to distorted moiré cells, rather than the local strain concentrated in the domain walls upon relaxation. Unlike other methods to estimate the large-scale heterostrain from the spatial structure of a moiré pattern [40], this DF TEM method includes knowledge of the lattice orientation and Burgers vector information, avoid-

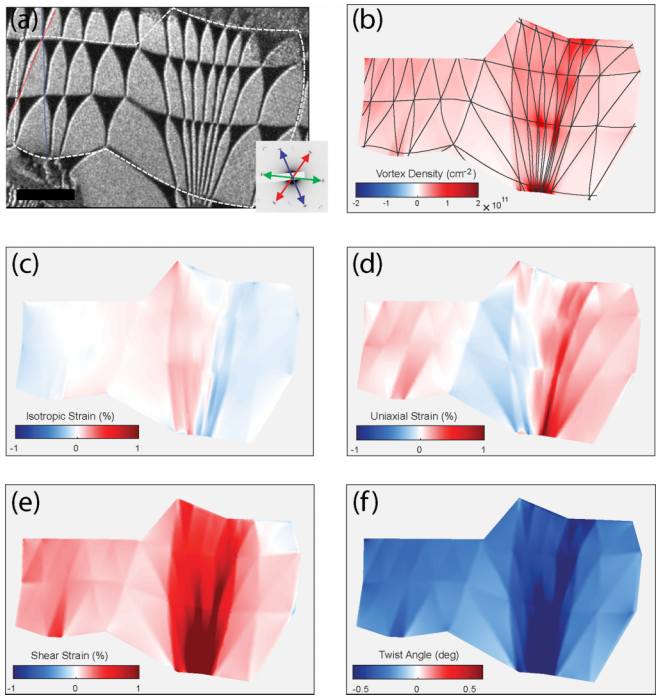

FIG. 8. (a) Dark field image of $WSe_2/MoSe_2$ heterobilayer, including domains larger than the lattice-mismatch limit. Scale bar is 100 nm. (Inset) Diffraction pattern from a nearby region and Burgers vectors. (b) Vortex density map. (c) Isotropic strain map showing average mismatch lower than the 0.3% expected from the intrinsic lattice mismatch. (d) Uniaxial strain map, showing opposite sign strain when domains are slanted left vs right. (e) Shear strain, showing magnitudes around 1% in the highly elongated domains. (f) Twist map, showing twist as the largest contributor to the moiré pattern.

ing the need to make additional assumptions. Still, the need to interpolate within the moiré cell means that information smaller than the moiré scale is not deterministic from the data. This method for strain mapping could supplement other experimental techniques that image the domain wall pattern in conjunction with Burgers vector information [41,42], to determine the large-scale strain distribution.

In Fig. 8, strain maps are shown for a heterostructure of $MoSe_2$ and WSe_2. The intrinsic lattice constant mismatch of 0.3% should show up in the isotropic component. However, isotropic mismatch smaller than 0.3% is measured, indicating that the lattice attains a global strain to achieve closer to epitaxial matching. As global lattice mismatch is often assumed to be fixed when calculating moiré lengths, this example illustrates how strain mapping can reveal useful information about the phenomenology of moiré materials.

V. CONCLUSION

In conclusion, we have presented a general and rigorous approach to describing the topology of nodes formed in moiré materials. Vortex and antivortex are described as the commutator $[a, b]$ and its inverse $[b, a]$ of the free group F_2 on generators a and b. The two generators have an intuitive geometric interpretation as two distinct ways by which to

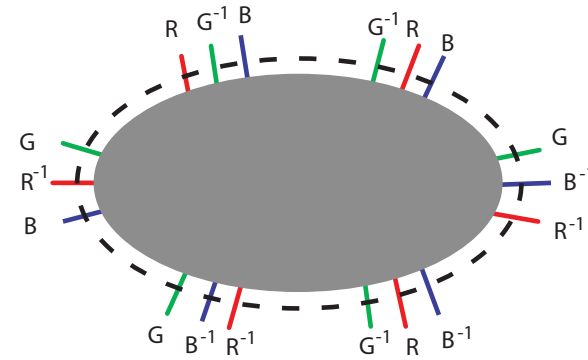

FIG. 9. General configuration of RGB lines extending from an arbitrary circle drawn on an experimentally TEM image. By writing out the RGB letters along the circumference of the circle, one can read off the total vorticity, number of dipoles, etc. contained in the circle.

make a transition from the AB to BA stacking order, and then back to AB. High-quality TEM measurements are then utilized to represent the abstract generators in terms of colors of domain walls, leading to a dictionary by which to infer the vortex content inside a given boundary. This dictionary relies upon the order in which the colored domain walls cross the boundary. The idea is schematically illustrated in Fig. 9.

We discover an antivortex-type node and present a DF TEM based method for characterizing the type of node and strain field, which does not rely on the usual assumption that the dominant component creating the moiré pattern is twist. This opens the door for the design and characterization of moiré materials based on anisotropic strain fields.

ACKNOWLEDGMENTS

We thank Frans Spaepen, David Nelson, and S.-W. Cheong for important discussions. P.K. acknowledges support from ARO MURI (W911NF-21-2-0147). R.E. acknowledges support from NSF DMR-1922172 for TEM analysis. H.Y. acknowledges the support by the National Research Foundation (NRF) grant funded by the Korean government (MSIT) (No. 2021R1C1C1010924). S.C. acknowledges support from NSF Grant No. OIA-1921199. P.C. acknowledges support from NSF DMS Award No. 1819220. M.L. acknowledges support from NSF DMREF Award No. 1922165. J.H. was supported by NRF-2019R1A6A1A10073079 and by EPIQS Moore theory centers at MIT and Harvard. He acknowledges the help of Manhyung Han for drawing the figures in Appendix and the discussion with Harry Baik on free group.

APPENDIX A: VORTEX ALGEBRA

We have avoided explicit use of the language of group theory in the main body of the paper. The two generators a, b and their commutators $[a, b]$, $[b, a]$ were introduced through physical motivation. Here we provide more in-depth discussion and generalizations based on the theory of the free group.

The fundamental group of the punctured torus is $F = F_2$, the free group on two generators a, b [36,37]. The a and b generators correspond to the two independent ways in which

one can encircle the torus. In an ordinary torus, the two operations a and b do commute (Abelian), and the only elements of the fundamental group of the torus are $a^m b^n$, which count the number of loops in both directions. For a punctured torus such commutativity is lost, and consequently the group structure becomes non-Abelian.

Elements of the free group F_2 consist of every conceivable sequence of "letters" such as $abaabbbaa\cdots$ called "words." Keep in mind that both letters a and b have specific geometric moves associated with them. At this point it is helpful to go over well-established theorems in free groups to guide our thinking.

We now use F to denote the original free group F_2. Given two elements $x, y \in F$, the commutator is denoted $[x, y] \equiv xyx^{-1}y^{-1}$. The "lower central series" of the free group can be defined as follows. One begins with $F^1 = F$ which is the original free group, then $F^2 = [F, F]$ is the subgroup of F consisting of all commutators $[x, y]$ and their products, i.e., all elements of the form

$$[x_1, y_1][x_2, y_2]\cdots[x_n, y_n], \ (x_i, y_i \in F).$$

The subgroup F^2 is also a normal subgroup, meaning that the quotient space F^1/F^2 is a group.

Now one can proceed inductively and define

$$F^n = [F, F^{n-1}],$$

the subgroup generated by all elements of the form $[x, y]$, where $x \in F$ and $y \in F^{n-1}$. It is easy to check from the definition that

$$F^1 \supset F^2 \supset F^3 \supset F^4 \cdots .$$

Much like the study of van der Waals materials, such "filtration" gives a nice way to study a free group structure "one layer at a time"!

Some facts that are worth noting about the lower central series are summarized.

(1) Any element f_1 of $F^1 = F$ can be uniquely written $a^{m_1} b^{n_1} f_2$ with $n_1, m_1 \in \mathbb{Z}$ and $f_2 \in F^2$.

(2) Any element f_2 of F^2 can be uniquely written $[a, b]^{m_2} f_3$ where $m_2 \in \mathbb{Z}$ and $f_3 \in F^3$.

(3) Any element f_3 of F^3 can be uniquely written $[a, [a, b]]^{m_3}[b, [a, b]]^{n_3} f_4$ with $m_3, n_3 \in \mathbb{Z}$ and $f_4 \in F^4$.

(4) Any element f_4 of F^4 can be uniquely written $([a, [a, [a, b]])^{m_4}([a, [b, [a, b]]])^{n_4}([b, [b, [a, b]]])^{p_4} f_5$ with $m_4, n_4, p_4 \in \mathbb{Z}$ and $f_5 \in F^5$.

By putting all of the above statements together, one sees that any element f in the free group can be uniquely written as

$$f = a^{m_1} b^{n_1} [a, b]^{m_2} [a, [a, b]]^{m_3} [b, [a, b]]^{n_3} ([a, [a, [a, b]]])^{m_4} ([a, [b, [a, b]]])^{n_4} ([b, [b, [a, b]]])^{p_4} f_5 \tag{A1}$$

and so on. In general, each F^k is a normal subgroup, and $F^k/F^{k+1} \simeq \mathbb{Z}^{r_k}$, meaning the quotient group is isomorphic to a product of r_k integer groups $\mathbb{Z} \times \cdots \times \mathbb{Z}$. The number of generators is r_k for a given quotient group F^k/F^{k+1}. Although the free group itself is non-Abelian, the quotient group F^k/F^{k+1} is Abelian, characterized by a set of r_k integers. These integers then go on to play the role of topological quantum numbers in physical contexts.

Elements of the free group (A1) for which $m_1 = n_1 = 0$ refer to closed loops in real-space graphical representation. It is clear that these are the only elements of F that we are interested in. Elements for which $f_5 = e$ (an identity) and $m_3 = n_3 = m_4 = n_4 = p_4 = 0$ are $f = [a, b]^{m_2}$ with nonzero m_2. These are the elements of the quotient group F^2/F^3 and represent the vortices ($m_2 > 0$) and antivortices ($m_2 < 0$) in physical contexts.

To consider higher-order topological defects, consider elements for which $f_5 = e$ and all integers in Eq. (A1) equal to zero except (m_3, n_3):

$$f = [a, [a, b]]^{m_3}[b, [a, b]]^{n_3}. \tag{A2}$$

Pictorial representations for the double commutators $[a, [a, b]]$, $[b, [a, b]]$ are easily obtained by tracing out paths according to definitions of a and b given in Fig. 6. We encourage readers to perform such exercises themselves and arrive at their graphical representations shown in Fig. 10. They are precisely the graphical representation of vortex-antivortex pairs (vortex dipoles) lying along the two crystallographic directions of the triangular lattice.

Next in line is the description of vortex quadrupole structure as triple commutators. According to Eq. (A1), there are only three generators of the quotient group $F^4/F^5 \simeq \mathbb{Z} \times \mathbb{Z} \times \mathbb{Z}$. How does one know there are only three generators at this level of filtration?

There is a theorem that gives the number of generators (r_k) at each level k through the formula

$$g^k = \sum_{d|k} d \cdot r_d. \tag{A3}$$

In this formula, the sum runs over all divisors d of the given integer k. For a free group with only two generators, we have $g = 2$ on the left side of the equation. To see how the formula works with $g = 2$, first set $k = 1$ to find $2 = r_1$. It means that the quotient group F^1/F^2 has two generators, namely a and b. At $k = 2$ we have $2^2 = r_1 + 2r_2 = 2 + 2r_2$ or $r_2 = 1$, hence there is only one generator of F^2/F^3 which is the commutator $[a, b]$. At $k = 3$ we have $2^3 = r_1 + 3r_3 = 2 + 3r_3$, and $r_3 = 2$ is the number of generators for F^3/F^4, namely $[a, [a, b]]$ and $[b, [a, b]]$. Finally, at $k = 4$, we get $2^4 = r_1 + 2r_2 + 4r_4 = 2 + 2 + 4r_4$, and $r_4 = 3$ is the number of generators of F^4/F^5 given by $[a, [a, [a, b]]]$, $[a, [b, [a, b]]]$, $[b, [b, [a, b]]]$. It is an arduous, but fun exercise to draw the real-space paths corresponding to each of the triple commutator. The results are the three distinct vortex quadrupole configurations in real space shown in Fig. 11.

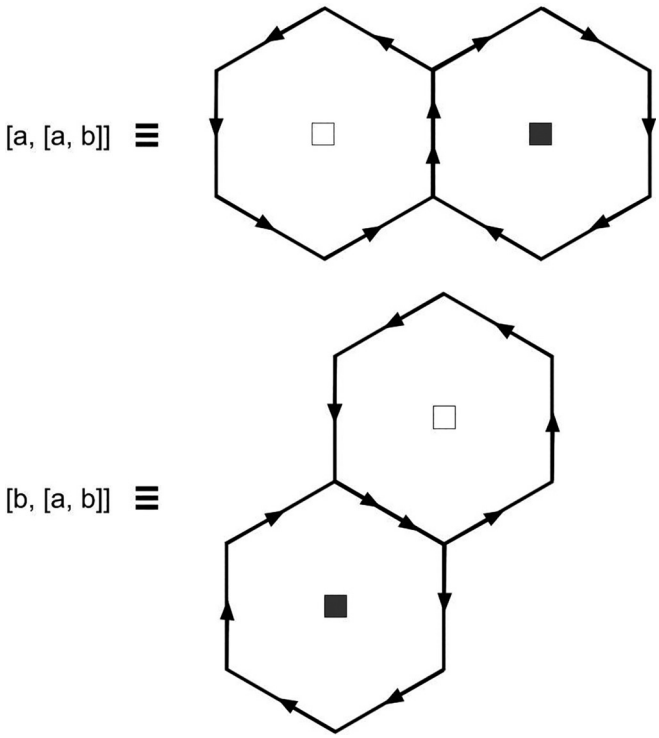

FIG. 10. Graphical representation of the double commutators $[a, [a, b]]$, $[b, [a, b]]$. They give vortex dipoles oriented along the two directions of the triangular lattice. Filled (empty) square is a vortex (anti-vortex).

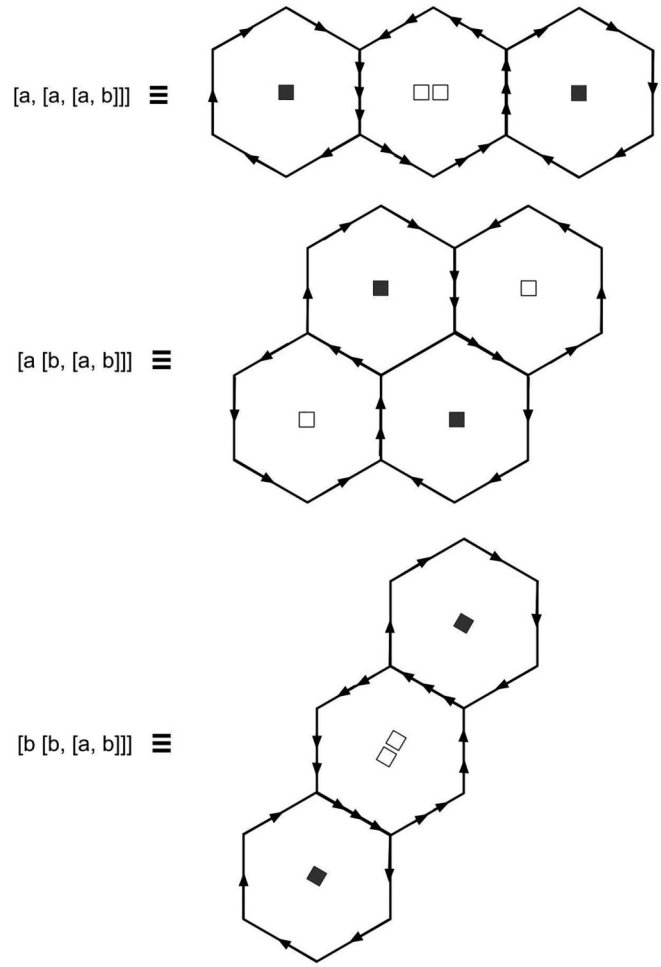

FIG. 11. Graphical representation of the three triple commutators $[a, [a, [a, b]]]$, $[a, [b, [a, b]]]$, $[b, [b, [a, b]]]$ correspond to three different kinds of vortex quadrupoles in real space.

APPENDIX B: RGB SCHEME FOR HIGHER-ORDER VORTICES

In Sec. III, we discussed ways to characterize a vorticity in terms of the RGB color scheme. A similar RGB scheme to characterize various higher-order vortex structures can be developed.

Figure 12 shows the vortex dipole and quadrupole configurations in terms of intersecting RGB loops. A small circle drawn around each intersection can determine the vorticity of that point. For instance, the filled (empty) circle round the top (bottom) intersection in Fig. 12(a) reads the product of letters $RG^{-1}BR^{-1}GB^{-1}$ ($BG^{-1}RB^{-1}GR^{-1}$) going counter-clockwise, corresponding to a vortex (an antivortex). Vortex quadrupole construction is done by having the three RGB loops intersect at four different points, as shown in Fig. 12(b). In both cases, a large circle drawn far away from the loops fails to cross any of the RGB lines.

It is possible to construct examples of vortex dipole configurations with loops extending out to infinity (hence crossing an arbitrary large circle) as in Figs. 13(a) and 13(b). The group elements assigned to each configuration can be calculated straightforwardly, leading to $[a, [b, a]]$ and $[ab, [b, a]]$ for the left and right configurations, respectively.

This kind of scheme is applicable to experimental situations. Draw a large loop enclosing a given TEM image in the manner shown in Fig. 9, then start counting the dislocation lines according to the *RGB* scheme. The RGB-based words can be converted to the *ab*-letter scheme with the help of the dictionary given in Eq. (10). The *ab*-based word can subsequently be converted to various commutators and higher-order commutators until it is cast in the general form given in Eq. (A1), from which the total vorticity, dipole numbers, quadrupole numbers and so on can be read off.

APPENDIX C: TEM IMAGE PROCESSING

TEM DF images were taken on a JEOL 2010F microscope, with 80kV accelerating voltage. A 5-μm objective aperture

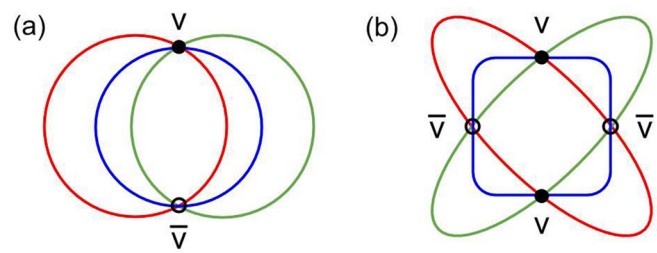

FIG. 12. (a) RGB graphical representation of a vortex dipole with v(vortex, filled circle) and $\overline{v}$(antivortex, empty circle) sites. (b) Quadrupole configuration with alternating $v\overline{v}v\overline{v}$ cores.

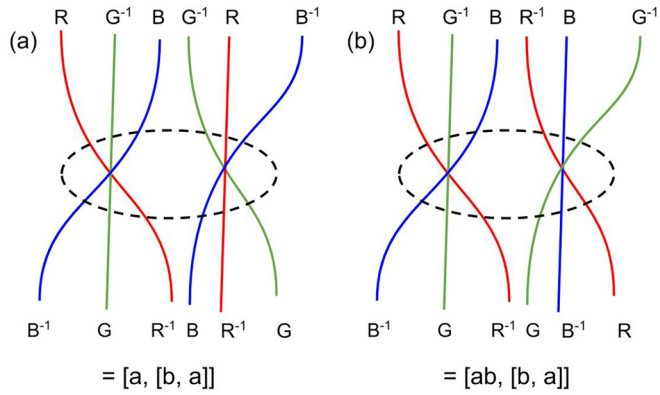

FIG. 13. (a) Extended vortex dipole configuration characterized by the letter sequence $RG^{-1}BG^{-1}RB^{-1}GR^{-1}BR^{-1}GB^{-1}$. After simple calculation, this becomes equivalent to $[a, [b, a]]$. (b) Another extended vortex dipole configuration, expressible as the double commutator $[ab, [b, a]]$.

was used to form the dark field images. RGB-colored composite images were formed using ADOBE PHOTOSHOP blending modes from three distinct second order images of a given sample region.

To create strain maps in Fig. 8, we performed image processing using PYTHON programming codes on images of red, blue, and green lines, such as in Fig. 7(b), to prepare to interpolate shift vector values. Ideally an algorithm could be created to extract the lines straight from TEM images but we skip that step for now, and manually trace the red, green, and blue lines to create an "ideal" (i.e., noiseless), but still raster, image. It is then necessary to split all lines into individual line segments and points of intersections, which we call nodes. First, using the connected Components function in PYTHON'S OPENCV library, nodes are found by searching for places where red, green, and blue pixels coincide. In a similar manner, pixels that belong to each red, green, or blue line are grouped into lists after dilating them to ensure continuity. We include each line in a dictionary that describes the color of the line and what nodes are part of it. Next, a circle centered around each node is removed from the image (set to R,G,B = 0,0,0), effectively breaking the lines into line segments. Again, the pixels of each segment are found and a dictionary is created for each line segment. The parent line of each segment is identified, as well as the nodes that are its endpoints.

Next, each node must be assigned three integer values corresponding to the coefficients of $\mathbf{a}_\mathrm{R}$, $\mathbf{a}_\mathrm{G}$, and $\mathbf{a}_\mathrm{B}$, where $\mathbf{a}_\mathrm{R}$ is the lattice vector associated with the red line, and so on. An origin node is picked arbitrarily and assigned the coefficients $(u_R, u_G, u_B) = (0, 0, 0)$. Then, a red segment adjacent to the starting node is chosen to reach a second node, which is assigned $(u_R, u_G, u_B) = (0, 1, -1)$. Now that a second node is assigned, the choices are not arbitrary because the direction of increase for each vector has been determined. Note that it is the case that $u_G + u_G + u_B = 0$ at every node, because $\mathbf{a}_\mathrm{R} + \mathbf{a}_\mathrm{G} + \mathbf{a}_\mathrm{B} = 0$. We also know that u_r is constant on red lines, u_g on green lines, etc. From each node, we move to its neighboring nodes (those connected by a segment), and use these properties to fill in the rest of the coefficients. A nice property of this manner of assigning coefficients is it does not need to be told whether a given point is a vortex or an antivortex. Lastly, using the csap and scipy libraries, we fit B-splines to each line segment while forcing the spline to pass through the nodes of the segment and then use the knots of the splines to generate a Gmsh mesh file.

The next part of the computation is done in the Julia programming language. The vector values of $\mathbf{a}_\mathrm{R}$ and $\mathbf{a}_\mathrm{G}$ (measured from a diffraction pattern) must be input ($\mathbf{a}_\mathrm{B}$ can be found from the other two). Recall that the vectors in the image plane should appear in the order of RGB while going clockwise to correctly distinguish vortices and antivortices. Coefficients are then attributed to points on lines of the mesh and interpolated via an elastic model using the Gridap library [43] and its interface with Gmsh [44]. The elastic model applies a cost to a large derivative in the u field, as well as a cost to deviating from the known values on the lines. The resulting u field is differentiated to get strain components. The values are defined on a mesh that is small compared to the moiré length. For plotting, the mesh values are interpolated onto a grid in the MATLAB software package.

In addition to spatially mapping each strain component, knowledge of the displacement gradient matrix can be used to map the density of vortices and antivortices. Antivortices are distinguished from vortices by the chirality of the rotation in configuration space as you make a loop in real space. To quantify the chirality, we can compare the sign of the cross product of a pair of real-space vectors to their corresponding vectors in configuration space. Consider the real space cartesian vectors $\mathbf{x}$ and $\mathbf{y}$ where $\mathbf{x} \times \mathbf{y}$ is positive. They correspond to $\overline{d}\mathbf{x}$ and $\overline{d}\mathbf{y}$ in configuration space, by Eq. (3). If the sign of the cross product in configuration space is also positive, it is a vortex. If negative, it is an antivortex.

Given that $\mathbf{x}$ and $\mathbf{y}$ are basis vectors and the matrix

$$\overline{d} = \begin{pmatrix} a & b \\ c & d \end{pmatrix} = \begin{pmatrix} \alpha + \beta & \gamma - \theta \\ \gamma + \theta & \alpha - \beta \end{pmatrix},$$

$\overline{d}\mathbf{x} \times \overline{d}\mathbf{y} = (ad - cb)xy$. Thus the condition for a vortex is $\det[\overline{d}] > 0$ and for antivortex is $\det[\overline{d}] < 0$.

Writing in terms of the strain components, the condition is

$$\mathrm{sgn}[(\alpha^2 + \theta^2) - (\beta^2 + \gamma^2)] = \begin{cases} 1 & \text{vortex} \\ -1 & \text{antivortex} \end{cases}. \quad \text{(C1)}$$

[1] L. Ponomarenko, R. Gorbachev, G. Yu, D. Elias, R. Jalil, A. Patel, A. Mishchenko, A. Mayorov, C. Woods, J. Wallbank *et al.*, Nature (London) **497**, 594 (2013).

[2] C. R. Dean, L. Wang, P. Maher, C. Forsythe, F. Ghahari, Y.Gao, J. Katoch, M. Ishigami, P. Moon, M. Koshino, T. Taniguchi, K. Watanabe, K. L. Shepard, J.Hone, and P. Kim, Nature (London) **497**, 598 (2013).

[3] B. Hunt, J. D. Sanchez-Yamagishi, A. F. Young, M. Yankowitz, B. J. LeRoy, K. Watanabe, T. Taniguchi, P. Moon, M. Koshino, P. Jarillo-Herrero, and R. C. Ashoori, Science **340**, 1427 (2013).

[4] R. V. Gorbachev, J. C. W. Song, G. L. Yu, A. V. Kretinin, F. Withers, Y. Cao, A. Mishchenko, I. V. Grigorieva, K. S. Novoselov, L. S. Levitov, and A. K. Geim, Science **346**, 448 (2014).

[5] K. Endo, K. Komatsu, T. Iwasaki, E. Watanabe, D. Tsuya, K. Watanabe, T. Taniguchi, Y. Noguchi, Y. Wakayama, Y. Morita, and S. Moriyama, Appl. Phys. Lett. **114**, 243105 (2019).

[6] Y. Cao, V. Fatemi, A. Demir, S. Fang, S. L. Tomarken, J. Y. Luo, J. D. Sanchez-Yamagishi, K. Watanabe, T. Taniguchi, E. Kaxiras, R. C. Ashoori, and P. Jarillo-Herrero, Nature (London) **556**, 80 (2018).

[7] Y. Cao, V. Fatemi, S. Fang, K. Watanabe, T. Taniguchi, E. Kaxiras, and P. Jarillo-Herrero, Nature (London) **556**, 43 (2018).

[8] G. W. Burg, J. Zhu, T. Taniguchi, K. Watanabe, A. H. MacDonald, and E. Tutuc, Phys. Rev. Lett. **123**, 197702 (2019).

[9] X. Liu, Z. Hao, E. Khalaf, J. Y. Lee, Y. Ronen, H. Yoo, D. Haei Najafabadi, K. Watanabe, T. Taniguchi, A. Vishwanath, and P. Kim, Nature (London) **583**, 221 (2020).

[10] C. Shen, Y. Chu, Q. Wu, N. Li, S. Wang, Y. Zhao, J. Tang, J. Liu, J. Tian, K. Watanabe, T. Taniguchi, R. Yang, Z. Y. Meng, D. Shi, O. V. Yazyev, and G. Zhang, Nat. Phys. **16**, 520 (2020).

[11] S. Chen, M. He, Y.-H. Zhang, V. Hsieh, Z. Fei, K. Watanabe, T. Taniguchi, D. H. Cobden, X. Xu, C. R. Dean, and M. Yankowitz, Nat. Phys. **17**, 374 (2021).

[12] S. Xu, M. M. A. Ezzi, N. Balakrishnan, A. Garcia-Ruiz, B. Tsim, C. Mullan, J. Barrier, N. Xin, B. A. Piot, T. Taniguchi, K. Watanabe, A. Carvalho, A. Mishchenko, A. K. Geim, V. I. Fal'ko, S. Adam, A. H. C. Neto, K. S. Novoselov, and Y. Shi, Nat. Phys. **17**, 619 (2021).

[13] H. Polshyn, J. Zhu, M. A. Kumar, Y. Zhang, F. Yang, C. L. Tschirhart, M. Serlin, K. Watanabe, T. Taniguchi, A. H. MacDonald, and A. F. Young, Nature (London) **588**, 66 (2020).

[14] X. Zhang, K.-T. Tsai, Z. Zhu, W. Ren, Y. Luo, S. Carr, M. Luskin, E. Kaxiras, and K. Wang, Phys. Rev. Lett. **127**, 166802 (2021).

[15] Z. Hao, A. M. Zimmerman, P. Ledwith, E. Khalaf, D. H. Najafabadi, K. Watanabe, T. Taniguchi, A. Vishwanath, and P. Kim, Science **371**, 1133 (2021).

[16] J. M. Park, Y. Cao, K. Watanabe, T. Taniguchi, and P. Jarillo-Herrero, Nature (London) **590**, 249 (2021).

[17] J. M. Park, Y. Cao, L.-Q. Xia, S. Sun, K. Watanabe, T. Taniguchi, and P. Jarillo-Herrero, Nat. Mater. **21**, 877 (2022).

[18] Y. Zhang, R. Polski, C. Lewandowski, A. Thomson, Y. Peng, Y. Choi, H. Kim, K. Watanabe, T. Taniguchi, J. Alicea, F. von Oppen, G. Refael, and S. Nadj-Perge, Science **377**, 1538 (2022).

[19] C. R. Woods, P. Ares, H. Nevison-Andrews, M. J. Holwill, R. Fabregas, F. Guinea, A. K. Geim, K. S. Novoselov, N. R. Walet, and L. Fumagalli, Nat. Commun. **12**, 347 (2021).

[20] L. An, X. Cai, D. Pei, M. Huang, Z. Wu, Z. Zhou, J. Lin, Z. Ying, Z. Ye, X. Feng, R. Gao, C. Cacho, M. Watson, Y. Chenb, and N. Wang, Nanoscale Horiz. **5**, 1309 (2020).

[21] X. Wang, K. Yasuda, Y. Zhang, S. Liu, K. Watanabe, T. Taniguchi, J. H. ad Liang Fu, and P. Jarillo-Herrero, Nat. Nanotechnol. **17**, 367 (2022).

[22] A. Weston, E. G. Castanon, V. Enaldiev, F. Ferreira, S. Bhattacharjee, S. Xu, H. Corte-León, Z. Wu, N. Clark, A. Summerfield, T. Hashimoto, Y. Gao, W. Wang, M. Hamer, H. Read, L. Fumagalli, A. V. Kretinin, S. J. Haigh, O. Kazakova, A. K. Geim, V. I. Fal'ko, and R. Gorbachev, Nat. Nanotechnol. **17**, 390 (2022).

[23] C. N. Lau, M. W. Bockrath, K. F. Mak, and F. Zhang, Nature (London) **602**, 41 (2022).

[24] A. Uri, S. Grover, Y. Cao, J. A. Crosse, K. Bagani, D. Rodan-Legrain, Y. Myasoedov, K. Watanabe, T. Taniguchi, P. Moon, M. Koshino, P. Jarillo-Herrero, and E. Zeldov, Nature (London) **581**, 47 (2020).

[25] J. H. Wilson, Y. Fu, S. Das Sarma, and J. H. Pixley, Phys. Rev. Res. **2**, 023325 (2020).

[26] Y. Bai, L. Zhou, J. Wang, W. Wu, L. J. McGilly, D. Halbertal, C. F. B. Lo, F. Liu, J. Ardelean, P. Rivera, N. R. Finney, X.-C. Yang, D. N. Basov, W. Yao, X. Xu, J. Hone, A. N. Pasupathy, and X.-Y. Zhu, Nat. Mater. **19**, 1124 (2020).

[27] H. Yoo, R. Engelke, S. Carr, S. Fang, K. Zhang, P. Cazeaux, S. H. Sung, R. Hovden, A. W. Tsen, T. Taniguchi, K. Watanabe, G.-C. Yi, M. Kim, M. Luskin, E. B. Tadmor, E. Kaxiras, and P. Kim, Nat. Mater. **18**, 448 (2019).

[28] J. S. Alden, A. W. Tsen, P. Y. Huang, R. Hovden, L. Brown, J. Park, D. A. Muller, and P. L. McEuen, Proc. Natl. Acad. Sci. USA **110**, 11256 (2013).

[29] S. Turkel, J. Swann, Z. Zhu, M. Christos, K. Watanabe, T. Taniguchi, S. Sachdev, M. S. Scheurer, E. Kaxiras, C. R. Dean, and A. N. Pasupathy, Science **376**, 193 (2022).

[30] Y. Yu, K. Zhang, H. Parks, M. Babar, S. Carr, I. M. Craig, M. V. Winkle, A. Lyssenko, T. Taniguchi, K. Watanabe, V. Viswanathan, and D. K. Bediako, Nat. Chem. **14**, 267 (2022).

[31] D. Thouless, *Topological Quantum Numbers in Nonrelativistic Physics* (World Scientific, 1998).

[32] N. D. Mermin, Rev. Mod. Phys. **51**, 591 (1979).

[33] S. Carr, D. Massatt, S. B. Torrisi, P. Cazeaux, M. Luskin, and E. Kaxiras, Phys. Rev. B **98**, 224102 (2018).

[34] J. Lin, W. Fang, W. Zhou, A. R. Lupin, J. C. Idrobo, J. Kong, S. J. Pennycook, and S. T. Pantelide, Nano Lett. **13**, 3262 (2013).

[35] K. O. Friedrichs, Ann. Math. **48**, 441 (1947).

[36] D. E. Cohen, *Combinatorial Group Theory: A Topological Approach (London Mathematical Society Student Texts, Series Number 14)* (Cambridge University Press, 1989).

[37] O. Kharlampovich and A. Myasnikov, J. Algebra **302**, 451 (2006).

[38] F. Guinea, M. I. Katsnelson, and A. K. Geim, Nat. Phys. **6**, 30 (2010).

[39] A. Sinner, P. A. Pantaléon, and F. Guinea, arXiv:2210.07262 (2022).

[40] D. Halbertal, S. Shabani, A. N. Passupathy, and D. N. Basov, ACS Nano **16**, 1471 (2022).

[41] N. P. Kazmierczak, M. V. Winkle, C. Ophus, K. C. Bustillo, S. Carr, H. G. Brown, J. Ciston, T. Taniguchi, K. Watanabe, and D. K. Bediako, Nat. Mater. **20**, 956 (2021).

[42] Y. Li, X. Wang, D. Tang, X. Wang, K. Watanabe, T. Taniguchi, D. R. Gamelin, D. H. Cobden, M. Yankowitz, X. Xu, and J. Li, Adv. Mater. **33**, 2105879 (2021).

[43] S. Badia and F. Verdugo, J. Open Source Software **5**, 2520 (2020).

[44] C. Geuzaine and J.-F. Remacle, Int. J. Numer. Meth. Engng. **79**, 1309 (2009).